Proceedings 10th NUMGE 2023
10th European Conference on Numerical Methods in Geotechnical Engineering
Zdravkovic L, Kontoe S, Taborda DMG, Tsiampousi A (eds)

https://doi.org/10.53243/NUMGE2023-112

Large deformation numerical analysis of rock permeability influence on anchor performance for offshore renewable applications

A. Genco[1], M. O. Ciantia[1], M. Brown[1], M. Previtali[1], A. Ivanovic[2] and N. Cresswell[3]

[1] *School of Science and Engineering, University of Dundee, Dundee, UK*
[2] *University of Aberdeen, Aberdeen, UK*
[3] *Swift Anchors, Edinburgh, UK*

ABSTRACT: The rapid expansion of Offshore Renewable Energy (ORE) is leading to the development of novel rock anchoring systems which require a reliable and efficient design method to operate under strong current and tidal action. Hydromechanical (HM) coupled processes, ultimately function of the loading rate and permeability of the rock are crucial for geotechnical design. As the experimental investigation of rock-structure HM interaction is challenging, numerical modelling is often the only alternative to advance the reliability of current empirical design methods. The Geotechnical Particle Finite Element Method (G-PFEM) is herein proposed to numerically assess the Rock Anchor (RA) response under axial loading in variable drainage conditions. A Structured Modified Cam Clay (S-MCC) constitutive model is adopted to represent the mechanical behaviour of a sandstone. By using a large strain non-local formulation, mesh dependency issues related to inevitable localisation processes are taken care of. Thanks to a fully HM coupled formulation the effect rock permeability on the evolution of excess pore water pressures and the mechanical response of a RA during axial pull-out is examined. The result show that these coupled HM effects play a substantial role on pull-out capacity of RA.

Keywords: G-PFEM; Offshore Geotechnical Engineering; Rock Anchors; Offshore Renewable Energy

1 INTRODUCTION

The deployment of offshore renewable energy is leading to the development of novel anchoring solutions. The tidal environment can however exert varying load conditions on floating devices, making the implementation of reliable and cost-efficient solutions challenging. As the optimization of the anchoring system can significantly reduce the overall cost of the tidal energy systems (Cresswell and Jeffcoate 2016) the ability to rigorously model the anchoring system is crucial. In deep water and hard rocky seabeds, Rock Anchors (RAs) represent an effective alternative to classic piled and gravity-based anchorages. The classic design procedures for RAs are highly conservative, as they are based on empirical relationships developed using onshore field tests requiring the assumption/identification of the cone pull-out expected failure mechanism (Yap and Rodger 1984, Weerasinghe and Littlejohn 1997, Kim and Cho 2012). To assess the rate effect on the pull-out capacity of RAs herein a parametric analysis was conducted varying the rock permeability. Depending on rock porosity and the presence of fractures/fissures, the permeability of rock can typically vary from 1×10^{-18} to 1×10^{-10} m^2 (Bagdassarov 2021). RAs will hence experience environmental loads causing the rock to sometimes respond in a drained, undrained and partially drained manner. As the water pressure distribution and its temporal evolution controls the effective stress distribution, Hydro-Mechanical (HM) coupled phenomena ultimately determine the failure mechanism. These HM coupled processes represent one of the main challenges for offshore geotechnical engineering as they are difficult to analyse through field or experimental physical modelling (Brown and Hyde 2008).

It is for this reason that advanced numerical methods are an attractive tool to support field and laboratory testing for the improvement of RA design. For example, the Limit Analysis (LA) simulations by Cerfontaine et al. (2021) showed why current design methods overestimate axial capacity of RAs by identifying the development of a deep failure mechanism. Genco et al. (2022) showed through a combination of the Finite Element Method (FEM) and LA that the associated flow rule assumption of LA strongly affects the overestimation of pull-out capacity. Despite these recent numerical advancements, RA HM coupled analyses in the literature are scarce. Only recently Genco et al. (2023) performed large strain HM coupled numerical simulations of the

axial response of RAs showing that considerable excess of pore water pression (*pwp)* distribution develops in the rock mass despite low loading rates. This work intends to systematically investigate HM effects on RA performance. To this end large strain HM coupled analyses are performed using the Geotechnical Particle Finite Element Method (G-PFEM). The finite strain formulation, coupled with the continuous remeshing framework employed by the numerical method is capable of overcoming mesh distortion limitations that usually affect classic continuum-based methods (Monforte et al. 2018, Carbonell et al. 2022). To overcome a mesh dependent response, a non-local finite strain formulation of a Structured Modified Cam Clay model (S-MCC) (Monforte et al. 2019) was used. The numerical results obtained confirm the strong control of the permeability rate effect on the RA response under tensile axial load. In some cases, rock dilation causes negative excess *pwp* that considerably influence the RA response. The variability of the interface friction is also investigated numerically showing a major influence on the RA ultimate capacity.

2 THE NUMERICAL MODEL

A novel RA designed for tidal offshore applications was modelled in G-PFEM to perform the rock permeability assessment. The anchor is made from steel and is a groutless concept composed of an upper shaft and drill head component (Cresswell and Jeffcoate 2016). The pull-out simulations were conducted in rock whilst varying the permeability values to estimate this effect on the RA axial response. Both frictional and smooth contacts were used in the analyses performed.

2.1 The G-PFEM

The G-PFEM is a continuum-based Updated Lagrangian framed method suitable for simulating large strain soil structure interaction problems (Monforte et al. 2017). The numerical method is open source and full details are reported in Carbonell et al. (2022b). The large strain formulation implemented provides the description of the motion computing static and kinematic variables referred to the last configuration performed (K. Bathe 1982). The domain is discretized to solve the classic equations as done in classic FEM, where the mesh nodes are considered as particles that can move during each calculation step (Figure 1). The boundary domain is also constantly updated during the analysis. Mesh distortion, which usually negatively affects classic FEMs simulations, is also solved by means of the remeshing technique. New particles are added in the region where the threshold of a defined plastic state variable is overcome, increasing the accuracy of the numerical solution (Monforte et al. 2017, Carbonell et al. 2022).

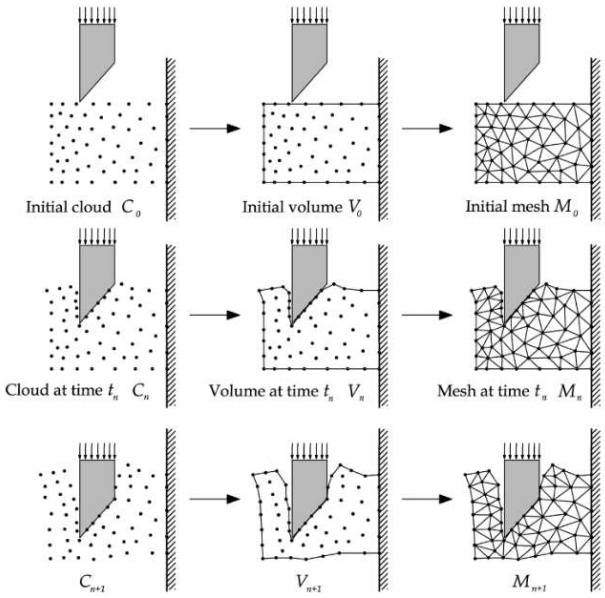

Figure 1. Sequence of mesh configurations represented by "cloud" of nodes updated during the calculation, simulating a stiff object penetrating in soil from Carbonell et al. (2022b)

Another important aspect handled by the G-PFEM is the strong mesh dependency effect which leads to no-objective results in brittle rocks that exhibit strong softening behaviour (Mánica et al. 2018). This numerical issue is fixed through a non-local approach where one or more state variables can be replicated by their nonlocal counterpart. This method harnesses the regularization technique by means of the internal length scale parameter (l_c) which prevent this dependency and controls the size of the localised region. The length scale parameter should be calibrated from the experimental perspective according to the thickness of the shear band and the level of softening (Oliynyk et al. 2021). In this work plastic strains are considered as non-local variables. A fully coupled formulation is attained through the mixed displacement Jacobian water pressure ($\boldsymbol{u}-\Theta-p_w$) formulation described by Monforte et al. (2017). In this way it is possible to describe the balance of mass and linear momentum equations for deformable multiple-phase porous media. The formulation is defined by the following equations:

$$\begin{cases} \nabla\cdot\left(\left(\breve{\boldsymbol{\sigma}}+P'\mathbb{I}\right)\right)+\boldsymbol{b}=0 & in\ \Omega_t\times(0,T) \\ J-\theta=0 & in\ \Omega_t\times(0,T) \\ -1/k_w\,\dot{p_w}+\nabla\cdot\boldsymbol{v}+\nabla\cdot\boldsymbol{v^d}=0 & in\ \Omega_t\times(0,T) \end{cases} \quad (1)$$

where $J=\det(\boldsymbol{F})$ and $\boldsymbol{F}$ is the total deformation gradient, $\breve{\boldsymbol{\sigma}}=\hat{\boldsymbol{\sigma}}\left(\breve{\boldsymbol{D}},V\right)$ with V the set of internal variables of the model, θ the volumetric deformation, $\boldsymbol{b}$ is the external body force tensor, $\partial\Omega_t=\Gamma_{pw}\cup\Gamma_g$ ($\Gamma_{pw}\cup\Gamma_g=\emptyset$) defines the boundary of the domain, P' is the effective Cauchy pressure, $\mathbb{I}$ stands for the second order identity tensor, p_w is the Cauchy water pressure ($\dot{p}_w=\frac{dp_w}{dt}$), k_w

is the water compressibility, $\boldsymbol{v}$ and $\boldsymbol{v^d}$ are the solid skeleton and Darcy's velocities, respectively. Further details on the mixed formulation are detailed in Monforte et al. (2017).

2.2 The structured Modified Cam Clay model

To model the rock and overcome a mesh dependent response, a non-local finite strain formulation of a structured MCC model (Monforte et al. 2019) is used. As for the original formulation, the yield locus shape is described by an ellipse and through a bonding related internal variable elastic states also in tension regime are permitted (Figure 2). The yield surface f and plastic potential g read:

$$\begin{cases} f(\boldsymbol{\tau}', P_s, P_t, P_m) = \left(Q/M(\theta)_f\right)^2 + P^*(P^* - P_c^*) \\ g(\boldsymbol{\tau}', p_s, p_t, p_m) = \left(Q/M(\theta)_g\right)^2 + P^*\left(P^* - P_{c,g}^*\right) \end{cases} \quad (2)$$

where $P' = tr(\boldsymbol{\tau}')/3$, $Q = \sqrt{3J_2}$ and θ represent the geotechnical stress invariants. M_f controls the vertical extent of the yield function in the Q:P Kirchhoff stress invariant space while M_g the slope of the Critical state line of the plastic potential function in the same Q:P space. P_t , P_s and P_m are internal hardening variables such that:

$$P_c^* = P_t + P_s + P_m = P_s + (1 + c)P_t \quad (3)$$

$$P^* = P' + P_t \quad (4)$$

where P_s acts as preconsolidation pressure of the reference unbonded material, whilst P_t and P_m (linear proportional through parameter c) indicate the tensile strength and the increase of the yield stress along the isotropic path respectively (Figure 2). These two hardening parameters control the evolution of the yield locus because the effect of the debonding process tends to zero for unstructured materials (Ciantia 2018). The hardening laws are defined as:

$$\dot{P}_s = \rho_s P_s \left((tr(\boldsymbol{l}^p) + \chi_s \sqrt{2/3}\, \|dev(\boldsymbol{l}^p)\| \right) \quad (5)$$

$$\dot{P}_t = -\rho_t P_t \left((tr(\boldsymbol{l}^p) + \chi_t \sqrt{2/3}\, \|dev(\boldsymbol{l}^p)\| \right) \quad (6)$$

where ρ_s, ρ_t, χ_s and χ_t are constitutive parameters and $\boldsymbol{l}^p = \partial g/\partial \boldsymbol{\tau}$ the spatial plastic velocity gradient which depends on $\boldsymbol{\tau}'$ the Kirchoff stress. Further details on the constitutive formulation are available from Monforte et al. (2019). The constitutive model was calibrated based upon triaxial test data on Berea sandstone provided by Wong et al. (1997). The calibration procedure was adopted following Ciantia and Di Prisco (2016).

The yield surface parameters were obtained matching the yield locus with experimental data in the triaxial plane. Whereas the elastic, plastic potential and hardening parameters were obtained using triaxial compression data in $Q - \varepsilon_a$ and $\varepsilon_{vol} - \varepsilon_a$ plots. The calibration procedure is further described in Genco et al. (2023). The final calibrated constitutive parameters are reported in Table 1.

Table 1. Constitutive parameters for the S-MCC model obtained from to the calibration procedure

E (MPa)	ν (-)	M_f (-)	M_g (-)	P_{s0} (MPa)	P_{t0} (MPa)
16800	0.20	1.00	1.25	200.00	5.00
P_m (MPa)	ρ_s (-)	ρ_t (-)	χ_s (-)	χ_t (-)	l_c (m)
180.00	14.00	14.00	0.10	0.00	0.01

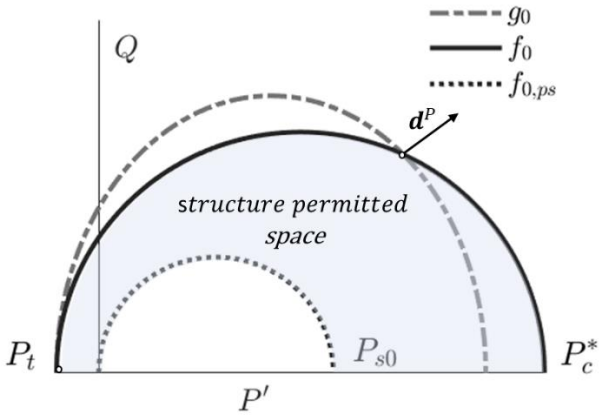

Figure 2. The yield locus and the plastic potential function for the structured MCC model

2.3 The Rock Anchor model

The geometry of the numerical problem is represented in Figure 3. The real RA size has not been stated for commercial reasons. The aforementioned RA is modelled by using rigid wall and the contact constraints are imposed by means of a penalty approach. The penalty parameter was set to avoid ill-conditioned numerical issues following Genco et al. (2023). An elastoplastic Coulomb law is used to describe the mechanical behaviour of rock-anchor interface. Both frictional and smooth interfaces were considered. For the steel-rock frictional contact, following Ziogos et al. (2021), an interface friction angle of δ=30° was used. The problem is assumed axisymmetric thus only a slice of the domain is represented. The model schematised in Figure 3 also shows the boundary conditions imposed for an embedment depth H/D of 6. This value was set to account the independence of the load capacity with the embedment depth following Genco et al. (2022). Initial *pwp* was set to zero in the whole domain while it was maintained at

0 MPa at the top boundary while no flow was permitted to all the other boundaries. The pull-out test was performed by applying a vertical displacement with a monotonic and constant rate of 0.01 m/s at the top of the anchor. This value was selected to reach 10%D displacement, which is commonly used in design practice to define the limit load, avoiding an excessive computational time. For this high rate of loading and typical rock permeability values, undrained behaviour is expected according to previous simulations performed.

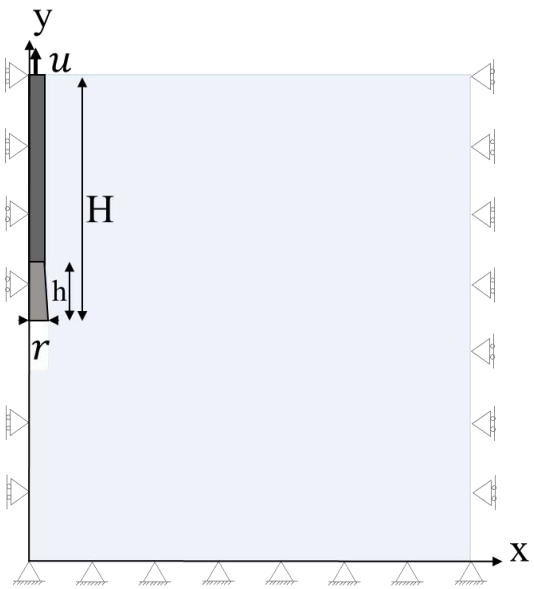

Figure 3. Geometry of the RA numerical model

3 NUMERICAL RESULTS

Numerical results on the influence of permeability on RA tensile capacity are presented in this section. The permeability of the rock is assumed isotropic and values are varied between 1×10^{-18} and 1×10^{-3} m/s in line with the experimental data on sandstone of Zhu and Wong (1997). The analyses also considered two different interface friction angles δ and Table 2 summarizes the set of simulations performed. All the results obtained are normalized by the reference case (δ=30° and $k = 1 \times 10^{-8}$) because of commercial sensitivity issues.

Table 2. Details of RA pull-out parameter simulations performed

δ (°)	k (m/s)	$\overline{F'}_{y\,max}$ (-)	$\overline{F'}_{x\,max}$ (-)	$\overline{U'}_{y\,max}$ (-)	$\overline{U'}_{x\,max}$ (-)
0	1×10^{-3}	0.095	1.167	5×10^{-6}	5×10^{-6}
0	1×10^{-5}	0.095	1.170	3×10^{-4}	3×10^{-4}
0	1×10^{-8}	0.098	1.163	0.112	0.098
0	1×10^{-12}	0.074	0.917	1.000	0.881
0	1×10^{-15}	0.074	0.917	0.966	0.870
0	1×10^{-18}	0.074	0.917	0.966	0.870
30	1×10^{-3}	0.972	0.967	5×10^{-6}	5×10^{-6}
30	1×10^{-5}	0.976	0.962	3×10^{-4}	3×10^{-4}
30	1×10^{-8}	1.000	1.000	0.098	0.104
30	1×10^{-12}	0.906	0.767	0.878	1.000
30	1×10^{-15}	0.911	0.774	0.867	0.966
30	1×10^{-18}	0.911	0.774	0.867	0.966

Figure 4 shows $\overline{F'}_y$ - *u/D* and a snapshot of the excess *pwp* distributions obtained in the simulation for the 1×10^{-5} m/s permeability case.

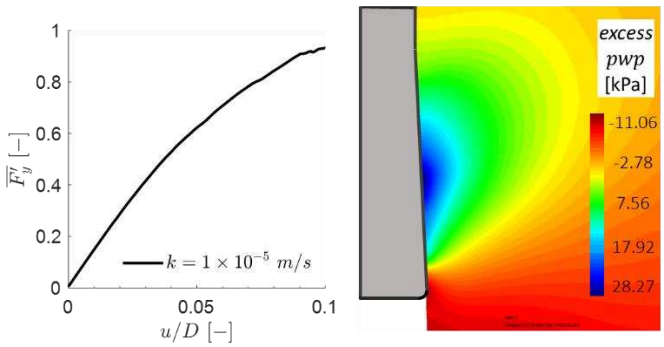

Figure 4. Force displacement curve and corresponding excess pwp contour plot at u=10%D

To represent the loading rate, a normalized pull-out velocity was used following Randolph and Hope, (2004):

$$V_c = vD/c_h = \frac{\lambda \gamma_w v D}{\sigma'_{v0}(1+e_0)k} \quad (8)$$

where v is the pull-out velocity, D the anchor diameter and c_h the horizontal coefficient of consolidation, λ the compressibility index, γ_w the bulk water density, e_0 the initial pore index, σ'_{v0} the effective vertical stress and k the permeability.

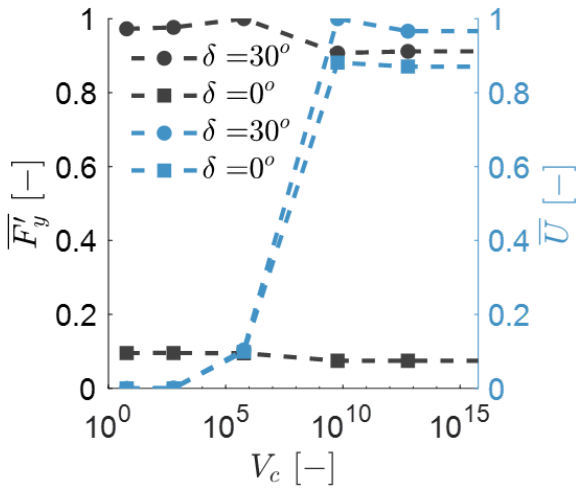

Figure 5. Effective pull-out capacity normalized (in black) and the excess pwp resultant nodal forces normalized (in blue) for $\delta = 30°$ and $\delta = 0°$ with normalized velocity according to Randolph and Hope, (2004)

Figure 5 summarises all the results from the parametric study. The effective normalized pull-out capacity ($\overline{F'}_y$) after 10%D of displacement is represented as a function of V_c. In the same plot the excess *pwp* resultant nodal force normalized by its maximum value ($\overline{U} = \sum_i^{i=n} \overline{U}_{n,i}$) acting on the anchor is also represented. The results highlight the clear influence of drained, partially drained, and undrained response on RA capacity. When the anchor is pulled at 0.01 m/s for normalized velocity values ranging from 5.9×10^5 to 5.9×10^9 the hydraulic regime is partially drained. The consolidation states are confirmed by plotting the $\overline{U}$. The interface friction angle does not influence the excess *pwp* resultant contact force distributions at the interface for drained loading while as the response moves to the undrained case, smooth rock-anchor interfaces show a 10% reduction of the $\overline{U}$ at the interface. The figure also shows that, as expected, δ affects the pull-out capacity. In particular, the reduction of about 90% of capacity is observed between frictional and smooth contact.

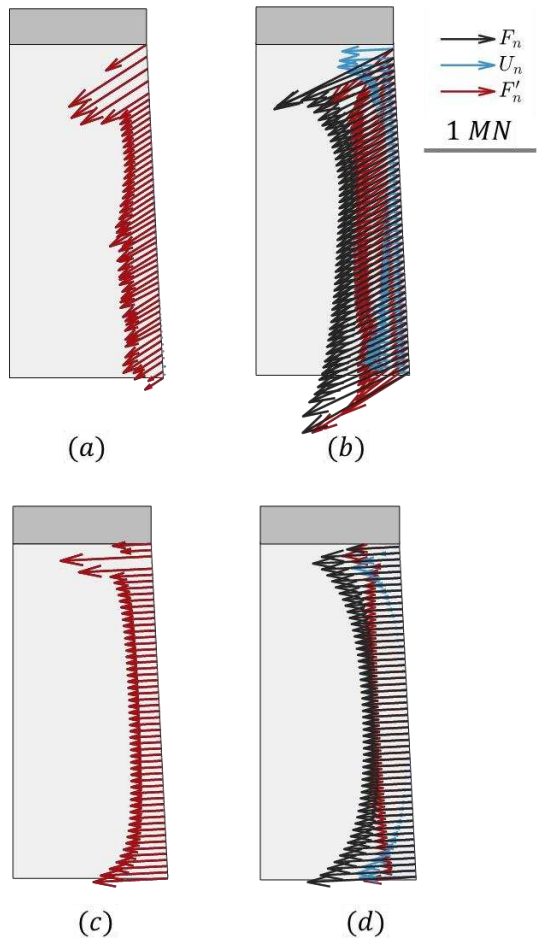

Figure 6. Distribution of the effective (F'_n) and total (F_n) nodal contact forces acting on the anchor along with pwp nodal forces (U_n) for $\delta = 30°$ (a, b) and $\delta = 0°$ (c, d) with rock permeability of $k = 1 \times 10^{-3}\ m/s$ (a, c) and $k = 1 \times 10^{-18}\ m/s$ (b, d) at the end of the simulation (u=10%D). Vectors of all components are represented to scale (1MN) in legend

Figure 6 shows the nodal contact force vectors acting on the anchor for both undrained and drained loading conditions. The results refer to both smooth and rough interfaces (δ=0° and δ=30°) after a displacement of $u = 10\%D$. The figure also shows the excess *pwp* nodal force distribution (U_n) acting on the anchor. Each *pwp* nodal forces (U_n) is the integral of the *pwp* over the corresponding segment on the anchor. For undrained loading U_n and in turn the excess *pwp* have a convex distribution with maximum values at the edges, regardless of the interface friction angle adopted. These features require further investigation that may be performed through systematic stress path analyses and excess *pwp* contour distribution evolution during the test.

4 CONCLUSIONS

In this paper the permeability effect on RA axial pull-out is systematically investigated numerically through large strain HM coupled G-PFEM simulations. A finite strain structured Modified Cam Clay model (S-MCC) is adopted to reproduce an intact sandstone rock. A parametric analysis of the rock permeability is carried out, while maintaining the load rate constant. This is equivalent to keeping the permeability constant but changing the loading rate. Through a normalized pull-out velocity, it was possible to identify drained, undrained and partially drained responses. The reduction of 10% on the pull-out capacity is observed between the fully drained and fully undrained regime for the type of rock examined. RA interface properties are also investigated showing the response is HM coupled as excess *pwp* distributions change for different interface friction angle. Contact force distributions and excess *pwp* acting on the anchor show interesting profiles that would require a more detailed investigation.

5 ACKNOWLEDGEMENTS

This research is part of an industry funded studentship (ETP EIDP #182). The technical and financial support of the industrial partner SWIFT ANCHORS and the financial support of the Engineering Technology Partnership (ETP) are gratefully acknowledged.

6 REFERENCES

Bagdassarov, N. 2021. Permeability of Rocks. Fundamentals of Rock Physics,: 178–210. Cambridge University Press. doi:10.1017/9781108380713.006.

Brown, M.J., and Hyde, A.F.L. 2008. Rate effects from pile shaft resistance measurements. Canadian Geotechnical Journal, **45**(3): 425–431. doi:10.1139/T07-115.

Carbonell, J.M., Monforte, L., Ciantia, M.O., Arroyo, M., and Gens, A. 2022. Geotechnical particle finite element method for modeling of soil-structure interaction under large deformation conditions. Journal of Rock

Mechanics and Geotechnical Engineering,. Chinese Academy of Sciences. doi:10.1016/J.JRMGE.2021.12.006.

Cerfontaine, B., Brown, M., Caton, A., Hunt, A., and Cresswell, N. 2021. Numerical modelling of rock anchor uplift capacity for offshore applications. doi:10.2/JQUERY.MIN.JS.

Ciantia, M.O. 2018. A constitutive model for the hydro-chemo-mechanical behaviour of chalk. Engineering in Chalk - Proceedings of the Chalk 2018 Conference, (January): 275–281. doi:10.1680/eiccf.64072.275.

Ciantia, M.O., and Di Prisco, C. 2016. Extension of plasticity theory to debonding, grain dissolution, and chemical damage of calcarenites. International Journal for Numerical and Analytical Methods in Geomechanics, **40**(3): 315–343. doi:10.1002/nag.2397.

Cresswell, and Jeffcoate. 2016. Anchor Installation for the Taut Moored Tidal Platform PLAT-O. 3rd Asian Wave and Tidal Energy Conference, (October 2016).

Genco, A., Ciantia, M.O., Ivanovic, M.B.A., Caton, A., and Cresswell, N. 2022. G-PFEM numerical investigation of rock anchor geometry on pull-out capacity for renewable offshore applications. (July): 1–2.

Genco, A., Ciantia, M.O., Previtali, M., Ivanovic, M.B.A., and Cresswell, N. 2023. G-PFEM numerical assessment of Rock Anchor interface properties on pull-out capacity for renewable offshore applications. (Under review)

K. Bathe. 1982. Finite Element Procedure.

Kim, H.K., and Cho, N.J. 2012. A design method to incur ductile failure of rock anchors subjected to tensile loads. Electronic Journal of Geotechnical Engineering, **17 T**: 2737–2746.

Mánica, M.A., Gens, A., Vaunat, J., and Ruiz, D.F. 2018. Nonlocal plasticity modelling of strain localisation in stiff clays. Computers and Geotechnics, **103**(July): 138–150. doi:10.1016/j.compgeo.2018.07.008.

Monforte, L., Arroyo, M., Carbonell, J.M., and Gens, A. 2018. Coupled effective stress analysis of insertion problems in geotechnics with the Particle Finite Element Method. Computers and Geotechnics, **101**(May): 114–129. Elsevier. doi:10.1016/j.compgeo.2018.04.002.

Monforte, L., Carbonell, J.M., Arroyo, M., and Gens, A. 2017. Performance of mixed formulations for the particle finite element method in soil mechanics problems. Computational Particle Mechanics, **4**(3): 269–284. Springer International Publishing. doi:10.1007/s40571-016-0145-0.

Monforte, L., Ciantia, M.O., Carbonell, J.M., Arroyo, M., and Gens, A. 2019. A stable mesh-independent approach for numerical modelling of structured soils at large strains. Computers and Geotechnics, **116**(August): 103215. Elsevier. doi:10.1016/j.compgeo.2019.103215.

Oliynyk, K., Ciantia, M.O., and Tamagnini, C. 2021. A finite deformation multiplicative plasticity model with non–local hardening for bonded geomaterials. Computers and Geotechnics, **137**: 104209. Elsevier. doi:10.1016/J.COMPGEO.2021.104209.

Weerasinghe, R.B., and Littlejohn, G.S. 1997. Uplift capacity of shallow anchorages in weak mudstone. *In* Ground anchorages and anchored structures. Proc. conference, London, 1997.

Wong, T., David, C., and Zhu, W. 1997. The transition from brittle faulting to cataclastic flow in porous sandstones: Mechanical deformation. Journal of Geophysical Research: Solid Earth, **102**(B2): 3009–3025. doi:10.1029/96jb03281.

Yap, L.P., and Rodger, A.A. 1984. A study of the behaviour of vertical rock anchors using the finite element method. International Journal of Rock Mechanics and Mining Sciences and, **21**(2): 47–61. doi:10.1016/0148-9062(84)91173-2.

Zhu, W., and Wong, T. 1997. The transition from brittle faulting to cataclastic flow: Permeability evolution. Journal of Geophysical Research: Solid Earth, **102**(B2): 3027–3041. doi:10.1029/96jb03282.

Ziogos, A., Brown, M.J., Ivanovic, A., and Morgan, N. 2021. Understanding rock–steel interface properties for use in offshore applications. Proceedings of the Institution of Civil Engineers - Geotechnical Engineering,: 1–15. doi:10.1680/jgeen.20.00183.